Groundwater

# An Application of Hydraulic Tomography to a Large-Scale Fractured Granite Site, Mizunami, Japan

by Yuanyuan Zha[1,2], Tian-Chyi J. Yeh[2], Walter A. Illman[3], Tatsuya Tanaka[4], Patrick Bruines[4], Hironori Onoe[5], Hiromitsu Saegusa[5], Deqiang Mao[6], Shinji Takeuchi[7], and Jet-Chau Wen[8,9]

## Abstract

While hydraulic tomography (HT) is a mature aquifer characterization technology, its applications to characterize hydrogeology of kilometer-scale fault and fracture zones are rare. This paper sequentially analyzes datasets from two new pumping tests as well as those from two previous pumping tests analyzed by Illman et al. (2009) at a fractured granite site in Mizunami, Japan. Results of this analysis show that datasets from two previous pumping tests at one side of a fault zone as used in the previous study led to inaccurate mapping of fracture and fault zones. Inclusion of the datasets from the two new pumping tests (one of which was conducted on the other side of the fault) yields locations of the fault zone consistent with those based on geological mapping. The new datasets also produce a detailed image of the irregular fault zone, which is not available from geological investigation alone and the previous study. As a result, we conclude that if prior knowledge about geological structures at a field site is considered during the design of HT surveys, valuable non-redundant datasets about the fracture and fault zones can be collected. Only with these non-redundant data sets, can HT then be a viable and robust tool for delineating fracture and fault distributions over kilometer scales, even when only a limited number of boreholes are available. In essence, this paper proves that HT is a new tool for geologists, geophysicists, and engineers for mapping large-scale fracture and fault zone distributions.

## Introduction

The characterization of detailed hydraulic properties of the fracture/fault zones is crucial to water resources and environmental issues. Approaches that quantitatively characterize hydraulic properties in fault zones and/or fractured rocks have evolved rapidly over the past few decades. For example, Hsieh et al. (1985) adopted a classical analytical solution based on an equivalent homogeneous media conceptual model to analyze data from 20 cross-hole pumping tests. They obtained anisotropy in $K$ for the bulk equivalent homogeneous fractured rock, without delineating the spatial distribution of hydraulic parameters and fractures. Using single- and multiple-well hydraulic tests at a site near Mirror Lake, New Hampshire, Hsieh et al. (1999) determined locations where fracture zones intersected individual boreholes and the degree of hydraulic connection between boreholes. At the same site, Day-Lewis et al. (2000) used a simulated-annealing algorithm to generate three-dimensional (3D) realizations of fracture-zone geometry conditioned to (1) borehole data, (2) inferred hydraulic connections between packer-isolated borehole intervals, and (3) an indicator (fracture zone or background $K$ bedrock) variogram model of spatial variability. Day-Lewis et al. (2003, 2006) subsequently combined geophysical data

[1]State Key Laboratory of Water Resources and Hydropower Engineering Science, Wuhan University, Wuhan, China.
[2]Department of Hydrology and Water Resources, University of Arizona, Tucson, AZ, USA.
[3]Department of Earth and Environmental Sciences, University of Waterloo, Waterloo, Ontario, Canada.
[4]Obayashi Corporation, Tokyo, Japan.
[5]Japan Atomic Energy Agency, Mizunami, Japan.
[6]Department of Geophysics, Colorado School of Mines, Golden, CO, USA.
[7]Department of Geosystem Sciences, Nihon University, Tokyo, Japan.
[8]Research Center for Soil and Water Resources and Natural Disaster Prevention, National Yunlin University of Science and Technology, Douliu, Taiwan.
[9]Corresponding author: Department of Safety, Health and Environmental Engineering, National Yunlin University of Science and Technology, Douliu 64002, Taiwan; 886-921-824183; fax: 886-5-537-6916; wenjc@yuntech.edu.tw

*Article Impact Statement*: Kilometer-scale hydraulic tomography can complement geological mapping to yield more detailed hydrogeological characteristics of fault zones.

Received August 2015, accepted March 2016.

doi: 10.1111/gwat.12421

and a conventional hydraulic test (a cross-hole test, not hydraulic tomography [HT]) as well as tracer tests at the site to characterize the fracture-rock aquifer heterogeneity.

After the 3D HT simulation work by Yeh and Liu (2000), HT laboratory experiment by Liu et al. (2002), and transient 3D HT analysis by Zhu and Yeh (2005), exploring the possibility of high-resolution mapping of fractured medium using HT, has become an active research area. For example, Brauchler et al. (2003) used HT to map the diffusivity of a single fracture in a large core sample through laboratory experiments. Hao et al. (2008), using numerical experiments, showed that HT can map the fracture pattern vividly, including its interconnectedness. Similarly, Ni and Yeh (2008) demonstrated the usefulness of pneumatic tomography (PT) for imaging fractures based on numerical experiments. More recently, Sharmeen et al. (2012) confirmed in the laboratory the efficacy of HT to detect fractures and their connectivity and reported that the estimated $K$ and $S_s$ could accurately predict the drawdown behavior in other pumping tests not used in the inverse modeling effort. Overall, the field applications of 3D HT work are still limited (Cardiff et al. 2013), and there are only a few HT field applications in fractured media (e.g., Lavenue and de Marsily 2001; Meier et al. 2001; Vesselinov et al. 2001; Illman et al. 2009; Tiedeman et al. 2010).

With a pilot point method, Lavenue and de Marsily (2001) analyzed datasets from seven boreholes induced by a series of sinusoidal pumping tests and available geologic facies data to characterize the $K$ field in the Culebra-fractured dolomite formation within the Delaware Basin in southeastern New Mexico. Likewise, Meier et al. (2001) interpreted drawdown and recovery datasets from seven boreholes induced by two cross-hole pumping tests and one steady-state head dataset during nonpumping periods to map preferential flow paths in a subvertical shear zone in granitic rock at the Grimsel rock laboratory (Switzerland). For mapping fractures in unsaturated media, Vesselinov et al. (2001) examined numerous cross-hole pneumatic injection tests at the Apache Leap Research Site (ALRS) in Arizona.

Based on the detailed site-scale subsurface stratigraphy in a fractured-aquifer in West Trenton, New Jersey, Tiedeman et al. (2010) developed a three-dimensional flow model consisting of predetermined 33 horizontal and inclined layers in addition to a known fault zone near a boundary. In line with the suggestion by Yeh and Lee (2007) for HT, they then took advantage of the groundwater level data collected at 44-48 monitoring wells or intervals due to temporary shutdown of three pumping wells in a pump-and-treat operation to calibrate the $K$ values of each layer of the model.

A recent comprehensive review by Illman (2014) emphasized that the accurate characterization of detailed distribution and the connectivity of fractures in a geological medium has been a technological challenge for decades. Based on many different studies conducted around the world, Illman (2014) concluded that HT offers much improved imaging of heterogeneity and, in particular, connectivity of hydraulic parameters in comparison to traditional mapping methods such as kriging, stochastic simulation, and stochastic inverse modeling of single-pumping tests.

Nonetheless, the scales of most of the previous investigations were limited to fractured media of meters to tens of meters. Very few cross-hole pumping or injection tests have been conducted in a tomographic fashion over thousands of meters in fault and/or fracture zones, except for those by the Japan Atomic Energy Agency (JAEA). During the past decade, JAEA installed several vertical and inclined boreholes over an area of several square kilometers at depths of up to 1 km to characterize the hydrogeology near the Mizunami Underground Research Laboratory (MIU) site in central Japan. The site is situated in a fractured and faulted granite formation (JAEA 2010). Two pumping tests during 2004-2005 were conducted at different depths along one borehole, and responses of the saturated granite formation were monitored using packed-off intervals at various depths within different boreholes.

With these datasets, Illman et al. (2009) estimated the hydraulic conductivity ($K$) and specific storage ($S_s$) tomograms as well as their uncertainties and delineated the large-scale connectivity of $K$ and $S_s$ at the site based on a sequential successive linear estimator (SSLE) (Zhu and Yeh 2005). They showed that the results of their analysis qualitatively corroborated well with observed drawdown records, available fault information, and coseismic groundwater level responses during several large earthquakes (e.g., Niwa and Takeuchi 2012). However, they suggested that estimated fracture pattern and fault locations may still involve large uncertainty due to only two pumping tests, with limited observations for inverse modeling.

Over the past few years, two large shafts for the underground laboratory were excavated at the MIU site. During the process of the excavation, groundwater was drained, and responses at all previously installed monitoring locations were monitored. In addition, a new pumping test was conducted in 2010 at a new borehole located at the vicinity of the shafts, and responses were collected with existing and additional observation boreholes. As these new datasets become available, we thus ask how much improvement can be obtained for the characterization of hydraulic parameter fields at the site as Illman et al. (2009) only used the data from two pumping tests. Furthermore, they used a uniform mesh and a relatively small computational domain, which may have led to undesirable boundary effects. Therefore, this paper aims to assess improvements of the estimated $K$ and $S_s$ fields and patterns of fractures and faults at the MIU site using all data collected with new pumping locations and new observation boreholes. It also studies the impacts of selected domain size and boundary conditions as well as prior geostatistical information.

## Description of the Field Site and Pumping Tests

A detailed description of the MIU site geology can be found in Saegusa and Matsuoka (2011). According

to the report, geological investigations have suggested that a prominent, low permeable fault zone, IF_SB3_02, runs through the MIU site with a North-North-West orientation and fracture lineaments along both sides of the faults (Figure 1). In addition, a low permeable zone exists between the Hongo Formation (AK/HG in Figure 1b) and the Toki Lignite-bearing Formation (TK). Toki Granite, which underlies the Toki Lignite-bearing formation, is highly fractured at depths between 300 and 500 m. Beneath the highly fractured unit (upper highly fractured domain: UHFD in Figure 1b) is a granitic body, which is less fractured (lower sparsely fractured domain: LSFD in Figure 1b) and extends to great depths. However, detailed hydrogeological characteristics of these fractures and faults are largely unknown.

There are nine vertical and slanted boreholes at the site (namely, MIZ-1, DH-2, DH-15, MSB-1, MSB-3, 10MI22, 05ME06, 07MI08 and 07MI09 around a main shaft [MS] and a ventilation shaft [VS] [Figure 1b]). MIZ-1 penetrates to a depth of 1300 m, DH-15 is about 1000 m deep, DH-2 is about 500 m in depth, and the other boreholes are shallow boreholes with lengths between 100 and 200 m. DH-15 is situated approximately 700 m southeast from the MIU site. In contrast, the average distance between the off-site borehole DH-2 and all the other on-site boreholes are less than 200 m. Observation boreholes (05ME06, 07MI08, and 07MI09) are spaced less than 50 m around MS and VS shafts, as shown in Figure 1b.

Three independent pumping tests (namely, tests 1, 2, and 4) were conducted at boreholes MIZ-1 and 10MI22 for characterizing the hydrogeology of the site. Nonetheless, during the course of excavation of the two vertical shafts (MS and VS), groundwater was continuously pumped at the two shafts, and groundwater responses were monitored. This dataset is treated as the responses of a pumping test (i.e., test 3).

Pumping locations, rates, and durations of these four tests are listed chronologically in Table 1. This table also lists the observation boreholes and intervals associated with each test. The observation boreholes are instrumented with multilevel monitoring systems. The numbers in the brackets after the borehole name in Table 1 denote the number of monitoring intervals (the higher the number, the deeper the observation interval) installed in each borehole.

Test 1 was conducted from December 14-28, 2004, at a depth interval of 191-226 m below the land surface along MIZ-1. Test 2 was conducted in the same borehole at a depth interval of 662-706 m from January 13 to 28, 2005. During these two tests, drawdowns were recorded in all observation intervals of boreholes DH-2, DH-15, MSB-1, and MSB-3. The datasets from tests 1 and 2 were analyzed by Illman et al. (2009), as mentioned previously.

Test 3 started on March 9, 2006 and continued for more than 4 years. Its drawdown responses were monitored at new depths along borehole MIZ-1 in addition to observation locations of tests 1 and 2. Pumping test 4 was conducted at a horizontal borehole, 10MI22, 304 m below the surface (Figure 1b), starting from August 11 to September 9, 2010. During test 4, drawdowns at three additional boreholes (05ME06, 07MI08 and 07MI09) were collected. It was noticed that the continuous drainage from the shafts (test 3) had created a large cone of depression and had influenced the responses of test 4. Nevertheless, the rates of decrease in heads at all observation intervals due to test 3 were almost constant, reaching a quasi-steady state prior to test 4. Accordingly, its effects on drawdowns observed during test 4 were estimated using data prior to test 4 and were removed. After this correction, we treated tests 3 and 4 as two independent tests.

Figure 2a is a 3D display of the pumping location of test 1 (upper interval of MIZ-1; 191-226 m deep) and monitoring intervals (shown as spheres) at different depths along boreholes DH-2, DH-15, MSB-1, and MSB-3. The drawdown-time curves recorded at these intervals are illustrated in Figure 2b, and they are color-coded according to the borehole. According to these well hydrographs (even though they fluctuated due to unknown factors), pressures at most of the intervals of MSB-1 and DH-15 apparently responded first; those of MSB-3 responded next; those of DH-2 lagged behind most; and two upper intervals of MSB-1 had the smallest drawdowns. Notice that DH-15 is located about 700 m horizontally away from the pumped interval, while DH-2 is about 260 m, and both MSB-1 and MSB-3 are about 120 m away. These fast and large and slow and small drawdown responses are also illustrated in Figure 2a, with large and small spheres at different observation intervals, with the colors corresponding to different boreholes. Evidently, monitoring intervals of DH-15, and MSB-1 must be well connected with the pumping interval (likely through fractures), except for the two upper intervals of MSB-1. While DH-2 is close to the pumping interval, drawdown responses at its monitoring intervals lagged behind. This appears to indicate that a low $K$ barrier likely exists between DH-2 and the pumping interval. Likewise, a low $K$ zone possibly separates the upper and lower intervals of MSB-1 and the pumped interval. Similar patterns of drawdown-time responses were observed at all the intervals during tests 2 and 4 (see Figures S1-S3, Supporting Information). These responses suggest that the pumped locations of tests 1, 2, and 4 are well connected to DH-15 and MSB-1, while they are isolated from DH-2, perhaps by a fault (IF_SB3_02), an inferred flow barrier based on various geological investigations.

The significance of drawdown responses along all boreholes during test 3 (dewatering of MS and VS) is illustrated in Figure 3a in a manner similar to that in Figure 2a. The color-coded drawdown-time curves and the total water drainage rates ($Q$) during the test are shown in Figure 3b. In contrast to responses during tests 1, 2, and 4, DH-15 and MSB-1 now had the smallest responses, MSB-3 had rapid and large responses, and the drawdowns in DH-2 followed. Note that even though some of the drawdowns fluctuated significantly due to variation in the drainage rate and unknown factors, differences in

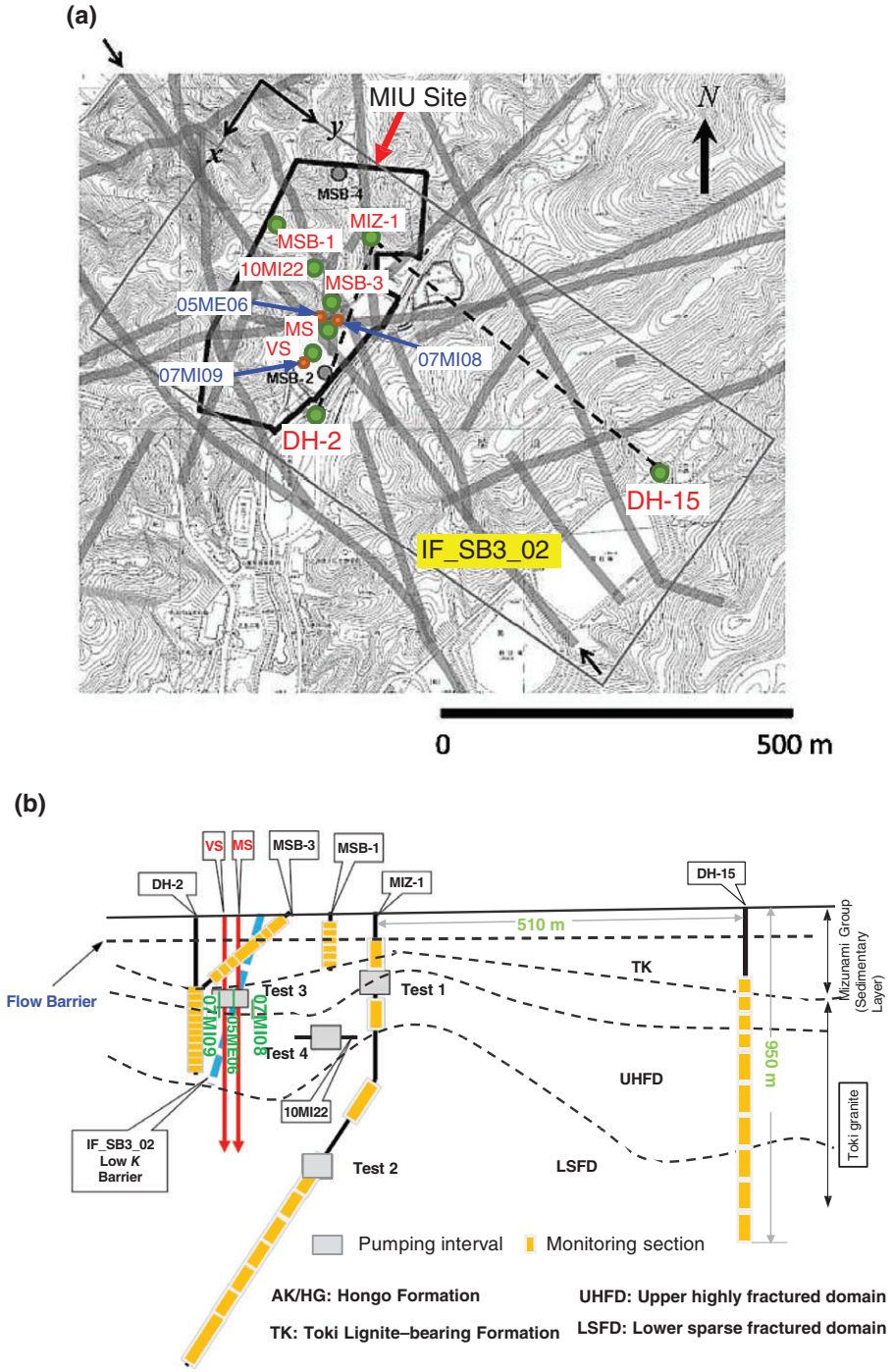


**Figure 1. (a) Map of lineaments and faults obtained on the basis of the geological and seismic surveys in the vicinity of the MIU site, where borehole locations as well as the locations of the main shafts (MS) and ventilation shafts (VS) are shown (modified from Illman et al. [2009]). (b) A schematic cross-section showing the boreholes, the pumped and observation intervals as well as the local geology along the dashed line connecting DH-1, MIZ-1, and DH-15 in a. The dashed curves approximately delineate the contact among various geological units.**

responses are apparent. As indicated by the sizes of the spheres in Figure 3a, responses at the observation intervals of MIZ-1 varied with their locations, in particular, large responses at deep intervals (for drawdown-time curve details, see Figure S17). Responses from this test suggest that the two shafts are likely linked with MSB-3 and DH-2 but separated from DH-15 and MSB-1, perhaps by the low $K$ barrier (IF_SB3_02).

## HT Analysis

To quantitatively interpret the observed groundwater responses during the four tests, we use the Simultaneous Successive Linear Estimator (SimSLE) algorithm (Xiang et al. 2009). SimSLE takes all the available pumping tests into consideration simultaneously to estimate the three-dimensional $K$ and $S_s$ spatial distributions as well as their

**Table 1**
**The Detail of the Four Pumping Tests**

| Test no. | Average pumping rate ($m^3/d$) | Period start | Period end | Pumping location(s) | | Observation intervals |
|---|---|---|---|---|---|---|
| | | | | Borehole name | Depth intervals (m) | |
| 1 | 14.4 | December 12, 2004 | December 28, 2004 | MIZ-1 | 191-226 | DH-2 (1-12)<br>DH-15 (1-10)<br>MSB-1 (1-5)<br>MSB-3 (1-7) |
| 2 | 7.2 | January 13, 2005 | January 28, 2005 | MIZ-1 | 662-706 | DH-2 (1-12)<br>DH-15 (1-10)<br>MSB-1 (1-5)<br>MSB-3 (1-7) |
| 3 | 558[1] | March 9, 2006 | — | MS&VS | Change with time | DH-2 (1-12)<br>DH15 (1-10)<br>MIZ1 (1-10)<br>MSB1 (1-5)<br>MSB3 (1-7) |
| 4 | 288 | August 11, 2010 | September 9, 2010 | 10MI22 | 304 | DH-2 (1, 5, 9, 12)<br>DH15 (1-10)<br>MIZ1 (1-3)<br>MSB1 (1-5)<br>MSB3 (1-7)<br>05ME06 (1-11)<br>07MI08 (1-7)<br>07MI09 (1-4) |

[1]The average pumping rate from MS and VS for the first 15 days.

uncertainties. The algorithm and the computational cost of SimSLE are presented in Supporting Information for interested readers.

### Data Utilized in the HT Analysis

Illman et al. (2009) excluded data that did not exhibit clear responses to pumping from the upper intervals of MSB-1 and MSB-3 during tests 1 and 2 because of their very small signal-to-noise ratios. However, we found that the upper intervals showed small but consistent responses during the four pumping tests. Thus, they were included in the current HT analysis. Although all tests lasted for a long period of time (Table 1), we only used data collected over the first 14 days for test 1 and 15 days for the other three tests. While drawdown data collected during longer pumping tests may carry information about heterogeneity at great distances, their usefulness for this investigation is limited. This is because most of the boreholes were clustered at the center of the MIU site (near field), and only a limited number of monitoring intervals were installed at one borehole (DH-15) at a far distance (far field). Thus, it would be difficult to interpret the large time drawdown as it likely represents the effects of heterogeneity anywhere within or beyond the simulation domain, unless more observation boreholes at different locations were available.

### Domain, Mesh, and Boundary Conditions

Different from the previous work (Illman et al. 2009), which employed uniform grids and a relatively small three-dimensional domain ($884 \times 392 \times 1054$ m), this analysis adopted a larger three-dimensional domain ($2000 \times 2000$ m in horizontal directions and 1400 m in the vertical direction). In addition, an adaptive mesh generator was developed to discretize the simulation domain. This irregular 3D mesh for the simulation is illustrated in Figure S4 along with the locations of the pumping and observation boreholes and intervals. This mesh discretization resulted in 43,470 nodes and 47,112 elements. The corresponding computational and storage costs for this inverse modeling effort are discussed in the Appendix S1.

For the HT analysis, we assumed that groundwater was hydrostatic prior to the beginning of each cross-hole pumping test. Constant head boundary conditions were assigned to the lateral boundaries, while the top and bottom were treated as no-flux boundaries. Diagnostic simulations indicated that different boundary conditions did not affect the inversion results as we deliberately selected a relatively large domain and short simulation times for the inversion.

### Prior Information

The prior information for SimSLE includes the mean $K$ and $S_s$ as well as their correlation scales. For this HT analysis, the guessed mean and variance values were the same as in Illman et al. (2009) (i.e., mean $K = 0.01$ m/d, mean $S_s = 2.3 \times 10^{-6}$ 1/m, variance of $\ln K = 2.0$, variance of $\ln S_s = 0.5$). The mean or effective $K$ and $S_s$ values (representing some average properties of

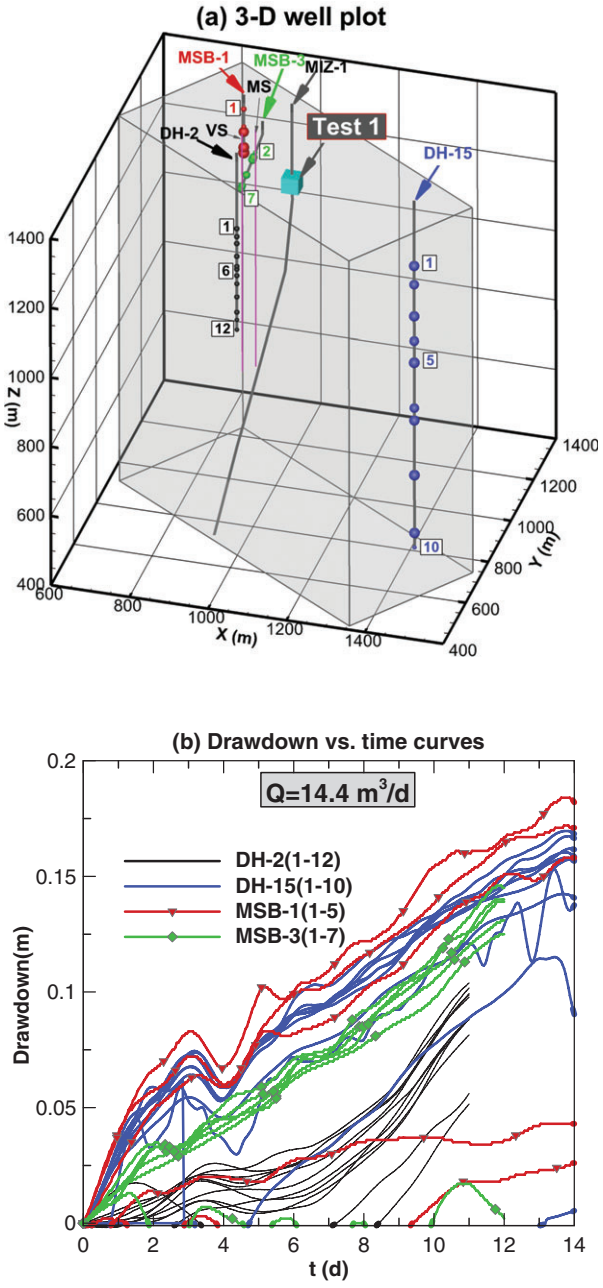


**Figure 2. Observed drawdown responses induced by cross-hole pumping test 1. (a) 3D borehole plot and (b) drawdown vs. time curve. In a, the size of the sphere reflects the relative significance of the drawdown recorded at each monitoring interval (see the interval number near the sphere) of each borehole. In b, the lines with the same color denote responses from different intervals of one borehole. The colors of the sphere correspond with the colors of the hydrographs. The cube indicates the pumped location. $Q$ is the pumping rate. More detailed drawdown curves are presented in Figure S15.**

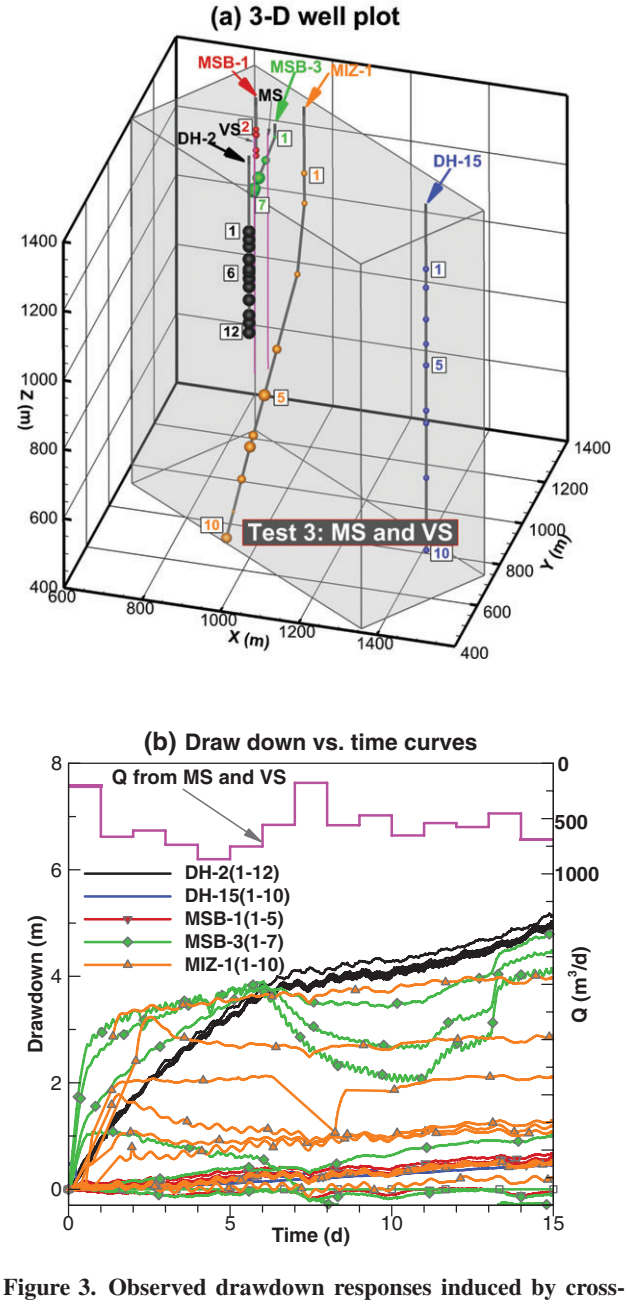


**Figure 3. Observed drawdown responses induced by cross-hole pumping test 3 (a) 3D borehole plot and (b) drawdown vs. time curve. In a, the size of the sphere reflects the relative significance of the drawdown recorded at each monitoring interval (see the interval number near the sphere) of each borehole. In b, the lines with the same color denote responses from different intervals of one borehole. The colors of the sphere correspond with the colors of the hydrographs. The cube indicates the pumped location. $Q$ is the pumping rate. More detailed drawdown curves are presented in Figure S17.**

matrix, fracture, and fault) were derived from traditional cross-hole pumping test analysis. Generally, such prior information, based on the unimodal distribution statistics, is often considered inadequate to characterize the bimodal distribution of $K$ for a fracture medium (e.g., Tsoflias et al. 2001). Nonetheless, according to Yeh and Liu (2000), prior information about mean, variance, and correlation scales does not play an important role in HT analysis for a porous medium if a large number of spatial observations (such as in HT analysis) are available. For fractured medium, the effects of initial estimates (means, variances, correlation scales, and correlation functions) had been investigated by Meier et al. (2001). They concluded that the large-scale heterogeneity patterns estimated from different initial guesses were similar but

could introduce great uncertainty when they were used in solute transport prediction. We also investigated the influence of initial guesses (shown in Figures S9-S10 in the Supporting Information), resulting in similar findings as those from Yeh and Liu (2000) and Meier et al. (2001).

## Results and Discussion

### Estimated Parameter Fields Using Data From Four Pumping Tests

According to Figure 4a, the HT analysis yielded two high $K$ zones and one low $K$ zone or barrier (relative to the mean or effective $K$ values). One of the high $K$ zones connects DH-15 and pumping boreholes of tests 1, 2, and 4; the other connects DH-2 (shallow borehole) and the lower part of MIZ-1 (deep borehole to more than 1000 m). These two high $K$ zones explain the observed drawdown behaviors in which DH-15 recorded large responses during tests 1, 2, and 4, while DH-2 registered large responses during test 3, and the lower part of MIZ-1 showed large responses during test 3. In addition, the locations of these high $K$ zones are geologically reasonable and, more importantly, are consistent with the general patterns of fracture lineaments mapped from geological investigations on both sides of the fault (Figure 1a).

A low $K$ fault zone (or barrier) with an irregular surface was depicted between the two high $K$ zones. It is close to the MS, and the lower part of the low $K$ fault zone is intruded by the high $K$ zone around the low part of MIZ-1. The location of this low $K$ fault zone generally agrees with the location of the fault (IF_SB3_02), which is thought to have low $K$ based on the geological investigation. However, the detailed spatial distribution is not entirely the same as that from the geological investigation (to be discussed in detail later). Nevertheless, we believe that the estimated low $K$ barrier represents the IF_SB3_02 fault.

In addition to the large-scale low $K$ fault, the joint inversion reveals that there is one small horizontal low $K$ zone located at the upper part of MSB-1 and MSB-3. The location of this horizontal low $K$ zone is also consistent with the contact between the Hongo Formation (AK/HG) and the Toki Lignite-bearing Formation (TK) presented in the geological cross section (Figure 1). Other figures for the estimated $K$ and $S_s$ fields and their related discussions can be found in the Supporting Information.

The above discussions are based on the isosurface map in Figure 4a. Cross-sectional views of the vertical slice cutting through DH-15 and MIZ-1, and that through DH-2 and the shafts, are illustrated in Figure 4b and 4c, respectively. These figures reveal that the high $K$ zones contain irregular fine-scale features, which explain observed different responses at different intervals at the same boreholes. For instance, the split of the upper and lower high $K$ zones (Figure 4a and 4c) is attributed to low responses at interval 4 of DH-15 during test 2 (see Figures S1a and S16).

### Impacts on Inversions From Different Datasets and Model Settings

The influences of adding new datasets on the estimated high $K$ zones are demonstrated in Figure 5a and 5c. Figure 5a shows that the data from the first two pumping tests (tests 1 and 2) reveal high $K$ zones that connect DH-15 and MIZ-1. As the data from test 3 are included, another high $K$ zone that connects DH-2 and the lower intervals of borehole MIZ-1 becomes apparent (Figure 5b). Additional information from test 4, however, does not yield new high $K$ zone, but the shapes of the high $K$ isosurfaces (or small-scale structures) have significantly changed (Figure 5c).

Figure 6a is a close-up view of the estimated low $K$ zones in three dimensions using all four tests. We first notice a horizontal low $K$ barrier near the top, which explains the small responses at the upper monitoring intervals of MSB-1 and MSB-3 during these tests. Then, we see a large vertical low $K$ barrier, which accounts for the slow and insignificant responses at DH-2 to the pumping in tests 1, 2, and 4 and minor responses at DH-15 during test 3. The transparent gray plane in these figures denotes the fault IF_SB3_02, estimated based on outcrop and information collected during the construction of inclined borehole MSB-3 and the main shaft. The location of the gray plane corresponds well with that of the vertical low $K$ zone.

Plan views of the estimated low $K$ zones (at $z = 1250$ m) using combinations of different tests are illustrated in Figure 6b. It shows that the estimated vertical low $K$ barrier ($K = 0.003$ m/d) based on the data from tests 1 and 2 is located on the left side of MIZ-1 and includes borehole DH-2, which is situated on the south side of the main shaft. This estimate is attributed to the fact that pumping locations (MIZ-1) of tests 1 and 2 are located on the same side of the fault and away from borehole DH-2. As a result, a low $K$ barrier of any shape between the pumping locations of tests 1 and 2 (MIZ-1) and DH-2 can mimic the observed response at DH-2 during these two pumping events.

Once the data from test 3 were included, the estimated vertical low $K$ barrier becomes narrower, and it is approximately located between the main shaft and the borehole MIZ-1. The strong and rapid responses at DH-2, when groundwater was drained from the two shafts, exclude the possibility that the low $K$ barrier is located between DH-2 and the two shafts. By the same token, the vertical low $K$ barrier must be located between borehole 10MI22 (pumped location of test 4) and the main shaft (MS) as DH-2 had few responses during test 4. The final location of the estimated vertical low $K$ barrier based on the inclusion of drawdown data from tests 1-4 thus agrees with the location of fault IF_SB3_02 based on geological interpretation.

Our estimated vertical low $K$ barrier, nevertheless, is somewhat different from the geological fault. As illustrated in Figure 1, geological interpretation suggests an inclined fault plane cutting through MS and VS and on the west side of MSB-1 and MSB-3. On the other

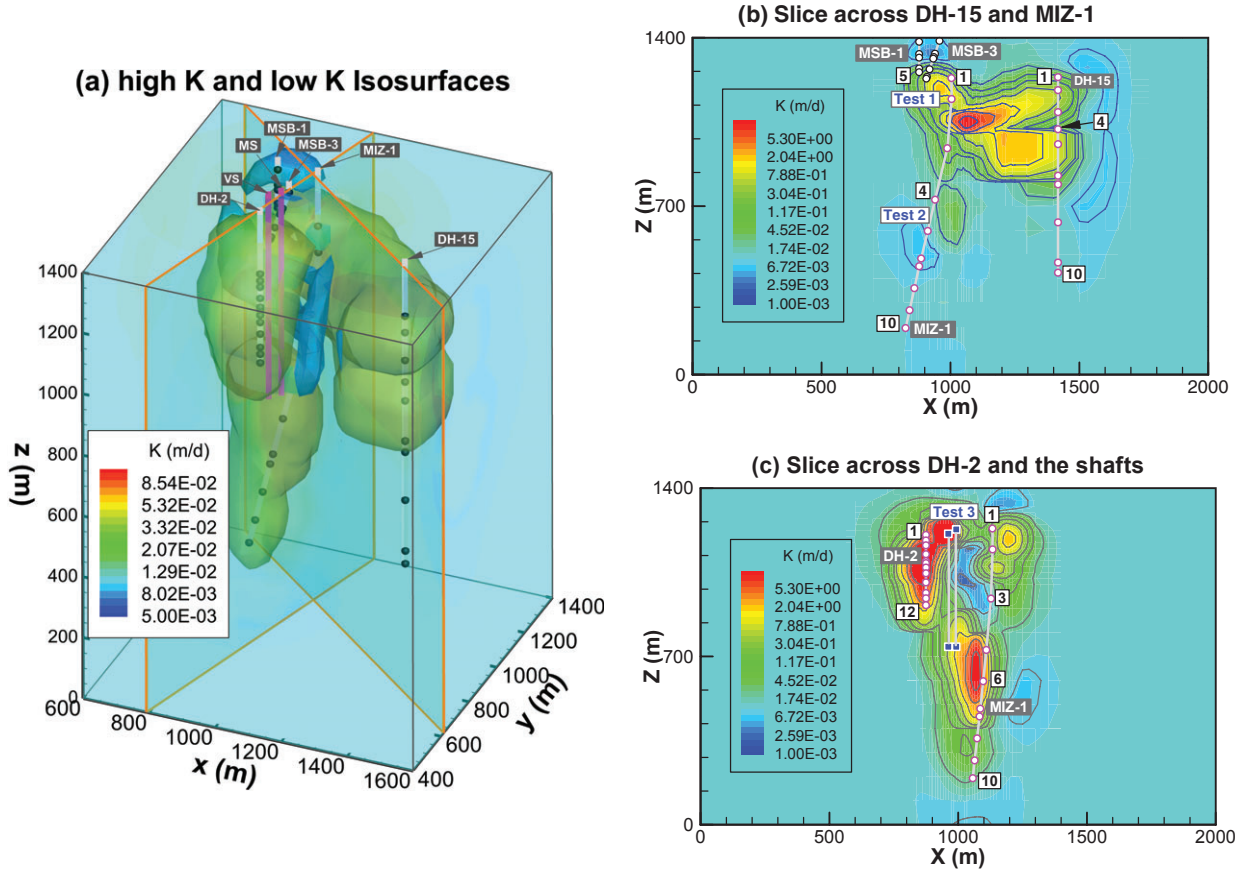


**Figure 4. The transient inversion results ($K$ tomogram) using data from tests 1, 2, 3, and 4, with (a) highlighted isosurfaces of $K = 0.06$ m/d (high $K$ zone) and $K = 0.003$ m/d (low $K$ zone), (b) slice cutting through DH-15 and MIZ-1, and (c) slice through DH-2 and MIZ-1. The cubes in (a) mark the locations of the pumping boreholes in tests 1, 2, and 4. The circles are the observation intervals numbered from top to bottom.**

hand, the estimated vertical low $K$ barrier using all the available data is highly irregular in shape and inclined, intercepting the main shaft, and running through the gap between MSB-1 and MSB-3. More importantly, our HT analysis shows that this low $K$ fault becomes thinner where the additional boreholes (05ME06, 07MI08, and 07MI09) are located.

Furthermore, responses at closely spaced boreholes (05ME06, 07MI08, and 07MI09) at test 4 (see Figure S3) allow mapping small-scale features of the heterogeneity. For instance, an opening (i.e., a high $K$ zone) is found in the middle of the vertical low $K$ barrier. This estimated "hole" is responsible for the observed rapid and significant responses observed in borehole 07MI08 (see Figure 5a), located at the west side of the low $K$ fault, and when the water was pumping from 10MI22, located at the east side of the low $K$ fault. Thus, it is probable that 07MI08 is connected to the pumped interval in 10MI22 of test 4 through small-scale fractures across the low $K$ fault. This finding suggests that our HT test and analysis yield additional information about the fault, which is not available through the geological investigation.

The uncertainty maps of the estimates using different subsets of data are also presented in Figures S13-S14. These figures show that the uncertainties of $K$ and $S_s$ are reduced at the regions where new pumping locations or observation boreholes are located.

Overall, our study shows that the connectivity between any two locations on either side of the fault (low permeable fault) can be substantiated only if the pumping tests are conducted on that side of the fault. For example, the estimated hydraulic properties on the west side of the fault remain ambiguous when only pumping tests 1 and 2 (at the east side) are considered, even though there are observation boreholes on both sides of fault. That is, if pumped locations are only located at one side of the barrier, signals are likely hindered by the barrier, and the responses will be very weak. Thus, we suggest that the pumping wells and observation boreholes should be installed on both sides of the fault based on geological and geophysical information. The distances between observation locations would determine the resolution of heterogeneity estimates, as concluded by Yeh and Liu (2000). This result suggests that prior geological or geophysical information is important to HT survey design (i.e., where the pumping and observation wells should be). Such that more detailed mapping of fractures and faults can be obtained.

The impacts on the inversions from two different model settings (the domains, meshes, and boundary

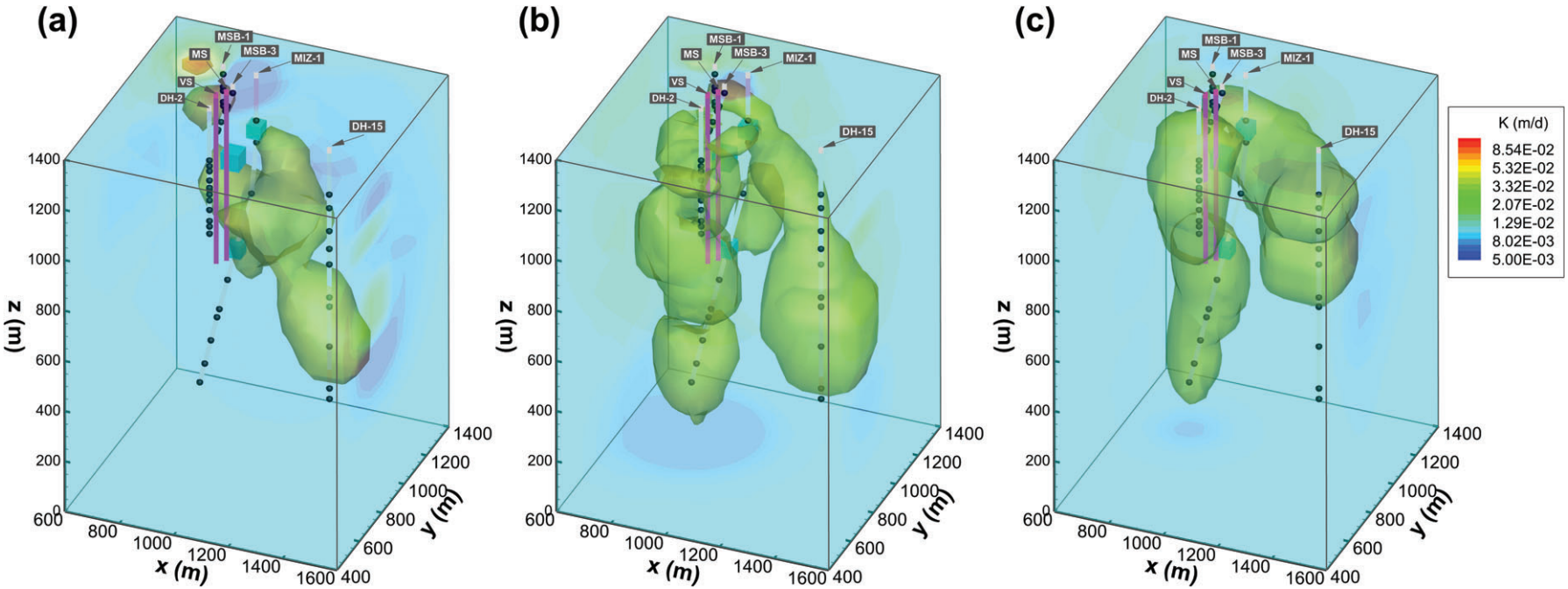


**Figure 5.** $K$ (m/d) tomograms obtained from the inversion of data from (a) tests 1 and 2, (b) tests 1-3, and (c) tests 1-4. Isosurface $K = 0.06$ m/d highlights the high $K$ zones. The cubes mark the locations of the pumping boreholes in tests 1, 2, and 4. The circles denote the locations of the observation intervals.

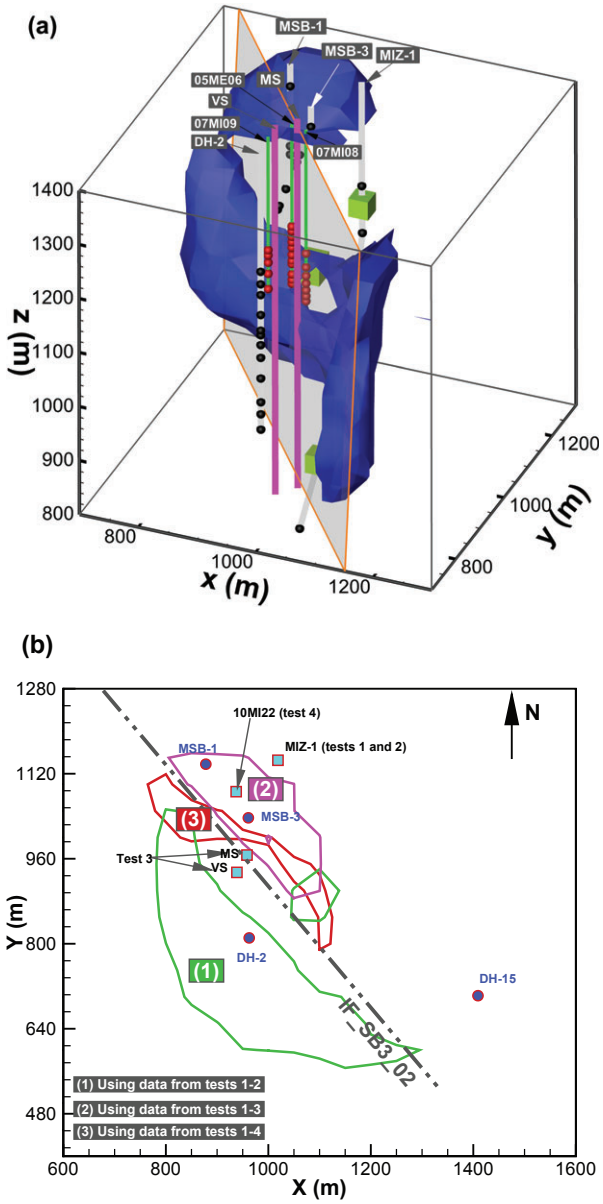


**Figure 6. (a) Isosurface $K = 0.003$ m/d (highlighting the low $K$ zone) obtained from the inversion of data from tests 1-4. The possible location of fault IF_SB3_02 is also presented. (b) The plan view ($z = 1250$ m) of the derived locations of the fault (low $K$ zone with $K = 0.003$ m/d) using different datasets and the geological location of the fault. Green fault is from the estimation using tests 1 and 2; pink fault is from the result using tests 1, 2, and 3; red fault is from the result using tests 1, 2, 3, and 4.**

conditions) used here and in Illman et al. (2009) are analyzed and presented in Figures S11-S12. We briefly mention here that the boundary conditions used in this study are more reasonable than those in Illman et al. (2009) as they allow us to reveal the low permeable layer near the top boundary based on geological information (Figure 1b). Moreover, the larger domain used here is helpful to minimize the boundary effect and suspicious high $K$ values in Illman et al. (2009).

## Conclusions

Illman et al. (2009) showed that HT is a promising tool to characterize fault/fractured zones with only few boreholes and two pumping tests. However, their pumping tests were conducted on the east side of a geologically mapped flow barrier (a fault zone). As a result, most features revealed by HT are limited to the east side, and the location of the barrier is uncertain, although it roughly agrees with that from geological investigation. Our analysis demonstrates that inclusion of new datasets from pumping test 3, which was conducted on the west side of the flow barrier, are crucial to map the correct location and depict irregular shape of the barrier and the fracture zone on the west side of the fault. Moreover, the additional data from test 4, close to the barrier illuminate, detailed the shape of the flow barrier and revealed some presence of preferential flow paths cross the flow barrier (Figure 6b). These results unambiguously stress the importance of consideration of prior geological information (fault zone) during the design of HT surveys, such that important non-redundant information can be collected to improve the resolution of HT estimates, corroborating the results from Yeh and Liu (2000); Wu et al. (2005); Illman et al. (2007); Huang et al. (2011); Berg and Illman (2011, 2013, 2015); Sun et al. (2013); Mao et al. (2013); and Yeh et al. (2014).

Our results also indicate that the inverse model domain, boundary conditions, and geostatistical prior information for inversion have some impacts on the estimates, which were not investigated in the study by Illman et al. (2009). Instead of assigning a constant head boundary at the top, as done by Illman et al. (2009), our use of lateral constant head boundary leads to geologically consistent results, confirming the suggestion by Sun et al. (2013) based on synthetic examples. A larger domain was proven useful to avoid suspicious boundary effect in the inversion. Furthermore, our analysis show that inversions based on different geostatistical prior information shared a common large-scale pattern but differed from each other in detailed shapes.

Despite the successful application of HT at the MIU site, it should be recognized that due to the highly discrete nature of fractures and faults, it is difficult to map their detailed distributions with a limited number of wells. Collecting more non-redundant information is necessary to increase the resolution (Bohling and Butler, 2010). Lastly, we concur with Bense et al. (2013) that synergistic efforts are required to gain a more integrated and comprehensive understanding of fault zone hydrogeology. The uncertainty maps obtained in this study can be used to guide the design of additional HT, geological, and geophysical surveys.

## Acknowledgments

This research was supported in part by the NSF EAR grant 1014594 and in part by the Strategic Environmental Research and Development Program (SERDP) under

grant ER-1365. Additional support for the project was provided to Walter A. Illman by the Natural Resources and Engineering Council of Canada (NSERC) through the Discovery grant. The first author acknowledges the support from National Natural Science Foundation of China (No. 51409192). J.-C. Wen would like to acknowledge the research support from NSC 101-2221-E-224-050, NSC 102-2221-E-224-050, MOST 103-2221-E-224-054, and MOST 104-2221-E-224-039 by the Minister of Science and Technology, Taiwan. T.-C.J. Yeh also acknowledges the Outstanding Overseas Professorship award through Jilin University by the Department of Education, China. We thank the three anonymous reviewers for their instructive and elaborate comments.

## Authors' Note

The authors does not have any conflicts of interest or financial disclosures to report.

## Supporting Information

Additional Supporting Information may be found in the online version of this article:

**Table S1.** The computational cost for SimSLE per iteration.
**Appendix S1.** Successive Linear Estimator algorithm.
**Appendix S2.** Drawdown responses.
**Appendix S3.** Computational cost of inverse modeling.
**Appendix S4.** Calibration and error issue.
**Appendix S5.** Estimated $K$ and $S_s$ from the joint inversion of the four tests.
**Appendix S6.** Influences of correlation functions.
**Appendix S7.** Influences of model settings.
**Appendix S8.** Uncertainty estimates.
**Appendix S9.** Detailed drawdown-time plots.
**Figure S1.** The drawdown responses during test 2 in a similar manner as those from tests 1 and 3 presented in the manuscript.
**Figure S2.** The drawdown responses during test 4 in a similar manner as those from tests 1 and 3 presented in the manuscript.
**Figure S3.** The drawdown responses during test 4 with additional observation wells (05ME06, 07MI08, 07MI09) in a similar manner as those from tests 1 and 3 presented in the manuscript.
**Figure S4.** The numerical domain and mesh.
**Figure S5.** The calibration map of the joint inversion for the four tests.
**Figure S6.** Displays the head calibration error and spatial variances of estimated $K$ and $S_s$ as functions of iterations during inversions.
**Figure S7.** The transient inversion results ($K$ estimates) based on the four tests.
**Figure S8.** The transient inversion results ($S_s$ estimates) based on the four tests.
**Figure S9.** The inverse $K$ estimates using large correlation scales (100 m, 100 m and 50 m, respectively).
**Figure S10.** The inverse $K$ results using the correlation function based on the information of the fault orientation.
**Figure S11.** The inverse results (K estimates) using tests 1 and 2 with different boundary conditions.
**Figure S12.** The inverse results (Ss estimates) using tests 1 and 2 with different boundary conditions.
**Figures S13.** The uncertainty maps of the K estimates using different pumping tests.
**Figure S14.** The uncertainty maps of the Ss estimates using different pumping tests.
**Figure S15.** Drawdown-time plots for different intervals of different observation boreholes induced by test 1.
**Figure S16.** Drawdown-time plots for different intervals of different observation boreholes induced by test 2.
**Figure S17.** Drawdown-time plots for different intervals of different observation boreholes induced by test 3.
**Figure S18.** Drawdown-time plots for different intervals of different observation boreholes induced by test 4.

## References

Bense, V.F., T. Gleeson, S.E. Loveless, O. Bour, and J. Scibek. 2013. Fault zone hydrogeology. *Earth-Science Review* 127: 171–192. DOI:10.1016/j.earscirev.2013.09.008.

Berg, S.J., and W.A. Illman. 2015. Comparison of hydraulic tomography with traditional methods at a highly heterogeneous site. *Groundwater* 53, no. 1: 71–89. DOI:10.1111/gwat.12159.

Berg, S.J., and W.A. Illman. 2013. Field study of subsurface heterogeneity with steady state hydraulic tomography. *Groundwater* 51, no. 1: 29–40. DOI:10.1111/j.1745-6584.2012.00914.x.

Berg, S.J., and W.A. Illman. 2011. Three-dimensional transient hydraulic tomography in a highly heterogeneous glaciofluvial aquifer-aquitard system. *Water Resources Research* 47: W10507. DOI:10.1029/2011WR010616.

Bohling, G., and J. Butler. 2010. Inherent limitations of hydraulic tomography. *Ground Water* 48, no. 6: 809–824. DOI:10.1111/j.1745-6584.2010.00757.x.

Brauchler, R., R. Liedl, and P. Dietrich. 2003. A travel time based hydraulic tomographic approach. *Water Resources Research* 39, no. 12: 1370. DOI:10.1029/2003WR002262.

Cardiff, M., W. Barrash, and P. Kitanidis. 2013. Hydraulic conductivity imaging from 3-D transient hydraulic tomography at several pumping/observation densities. *Water Resources Research* 49, no. 11: 7311–7326. DOI:10.1002/wrcr.20519.

Day-Lewis, F.D., J.W. Lane, and S.M. Gorelick. 2006. Combined interpretation of radar, hydraulic, and tracer data from a fractured-rock aquifer near Mirror Lake, New Hampshire, USA. *Hydrogeology Journal* 14, no. 1–2: 1–14. DOI:10.1007/s10040-004-0372-y.

Day-Lewis, F.D., J.W.L. Jr., J.M. Harris, and S.M. Gorelick. 2003. Time-lapse imaging of saline-tracer transport in fractured rock using difference-attenuation radar tomography. *Water Resources Research* 39, no. 10: 1290. DOI:10.1029/2002WR001722.

Day-Lewis, F.D., P.A. Hsieh, and S.M. Gorelick. 2000. Identifying fracture-zone geometry using simulated annealing and hydraulic-connection data. *Water Resources Research* 36, no. 7: 1707. DOI:10.1029/2000WR900073.

Hao, Y., T.-C.J. Yeh, J. Xiang, W.A. Illman, K. Ando, K.-C. Hsu, and C.-H. Lee. 2008. Hydraulic tomography for detecting fracture zone connectivity. *Ground Water* 46, no. 2: 183–192. DOI:10.1111/j.1745-6584.2007.00388.x.

Hsieh, P.A., A.M. Shapiro, and C.R. Tiedeman. 1999. Computer simulation of fluid flow in fractured rocks at the mirror

lake FSE well field, in *U.S. Geological Survey Toxic Substances Hydrology Program—Proceedings of the Technical Meeting*, vol. 3, ed. D.W. Morganwalp and H.T. Buxton, 777–781. Subsurface contamination from point sources. U.S. Geological Survey Water-Resources Investigations Report 99-4018C, Charleston South Carolina.

Hsieh, P.A., S.P. Neuman, G.K. Stiles, and E.S. Simpson. 1985. Field determination of the three-dimensional hydraulic conductivity tensor of anisotropic media 2. Methodology and application to fractured rocks. *Water Resources Research* 21, no. 11: 1667–1676. DOI:10.1029/WR021i011p01667.

Huang, S.-Y., J.-C. Wen, T.-C.J. Yeh, W. Lu, H.-L. Juan, C.-M. Tseng, J.-H. Lee, and K.-C. Chang. 2011. Robustness of joint interpretation of sequential pumping tests: Numerical and field experiments. *Water Resources Research* 47, no. 10: W10530. DOI:10.1029/2011WR010698.

Illman, W.A. 2014. Hydraulic tomography offers improved imaging of heterogeneity in fractured rocks. *Groundwater* 52, no. 5: 659–684. DOI:10.1111/gwat.12119.

Illman, W.A., X. Liu, S. Takeuchi, T.-C.C.J. Yeh, K. Ando, and H. Saegusa. 2009. Hydraulic tomography in fractured granite: Mizunami underground research site, Japan. *Water Resources Research* 45, no. 1: W01406. DOI:10.1029/2007WR006715.

Illman, W.A., X. Liu, and A. Craig. 2007. Steady-state hydraulic tomography in a laboratory aquifer with deterministic heterogeneity: Multi-method and multiscale validation of hydraulic conductivity tomograms. *Journal of Hydrology* 341, no. 3–4: 222–234. DOI:10.1016/j.jhydrol.2007.05.011.

Japan Atomic Energy Agency. 2010. Master Plan of the Mizunami Underground Research Laboratory Project, JAEA-Review 010–016.

Lavenue, M., and G. de Marsily. 2001. Three-dimensional interference test interpretation in a fractured aquifer using the Pilot Point Inverse Method. *Water Resources Research* 37, no. 11: 2659–2675.

Liu, S., T.-C.J. Yeh, and R. Gardiner. 2002. Effectiveness of hydraulic tomography: Sandbox experiments. *Water Resources Research* 38, no. 4: 5–1–5–9. DOI:10.1029/2001WR000338.

Mao, D., T.-C.J. Yeh, L. Wan, J.-C. Wen, W. Lu, C.-H. Lee, and K.-C. Hsu. 2013. Cross-correlation analysis and information content of observed heads during pumping in unconfined aquifers. *Water Resources Research* 49, no. 4: 1782–1796. DOI:10.1002/wrcr.20066.

Meier, P., A. Medina, and J. Carrera. 2001. Geostatistical inversion of cross-hole pumping tests for identifying preferential flow channels within a shear zone. *Groundwater* 39, no. I: 10–17. DOI:10.1111/j.1745-6584.2001.tb00346.x.

Ni, C.-F., and T.-C.J. Yeh. 2008. Stochastic inversion of pneumatic cross-hole tests and barometric pressure fluctuations in heterogeneous unsaturated formations. *Advances in Water Resources* 31, no. 12: 1708–1718. DOI:10.1016/j.advwatres.2008.08.007.

Niwa, M., and R. Takeuchi. 2012. Groundwater pressure changes in Central Japan induced by the 2011 off the Pacific coast of Tohoku Earthquake. *Geochemistry, Geophysics, Geosystems* 13, no. 5: Q05020. DOI:10.1029/2012GC004052.

Saegusa, H., and T. Matsuoka. 2011. Final report on the surface-based investigation phase (phase 1) at the Mizunami Underground Research Laboratory project, JAEA-Research 2010-067 Ibaraki, Japan.

Sharmeen, R., W.A. Illman, S.J. Berg, T.-C.J. Yeh, Y.-J. Park, E.A. Sudicky, and K. Ando. 2012. Transient hydraulic tomography in a fractured dolostone: Laboratory rock block experiments. *Water Resources Research* 48, no. 10: W10532. DOI:10.1029/2012WR012216.

Sun, R., T.-C.J. Yeh, D. Mao, M. Jin, W. Lu, and Y. Hao. 2013. A temporal sampling strategy for hydraulic tomography analysis. *Water Resources Research* 49, no. 7: 3881–3896. DOI:10.1002/wrcr.20337.

Tiedeman, C.R., P.J. Lacombe, and D.J. Goode. 2010. Multiple well-shutdown tests and site-scale flow simulation in fractured rocks. *Ground Water* 48, no. 3: 401–415. DOI:10.1111/j.1745-6584.2009.00651.x.

Tsoflias, G.P., T. Halihan, and J.M. Sharp. 2001. Monitoring pumping test response in a fractured aquifer using ground-penetrating radar of monitoring. *Water Resources Research* 37, no. 5: 1221–1229.

Vesselinov, V.V., S.P. Neuman, and W.A. Illman. 2001. Three-dimensional numerical inversion of pneumatic cross-hole tests in unsaturated fractured tuff 2. Equivalent parameters, high-resolution stochastic imaging and scale effects. *Water Resources Research* 37, no. 12: 3019–3041. DOI:10.1029/2000WR000135.

Wu, C.-M., T.-C.J. Yeh, J. Zhu, T.H. Lee, N.-S. Hsu, C.-H. Chen, and A.F. Sancho. 2005. Traditional analysis of aquifer tests: Comparing apples to oranges? *Water Resources Research* 41, no. 9: W09402. DOI:10.1029/2004WR003717.

Xiang, J., T.-C.J. Yeh, C.-H. Lee, K.-C. Hsu, and J.-C. Wen. 2009. A simultaneous successive linear estimator and a guide for hydraulic tomography analysis. *Water Resources Research* 45, no. 2: W02432. DOI:10.1029/2008WR007180.

Yeh, T.-C.J., D. Mao, Y. Zha, K.-C.C. Hsu, C.-H.H. Lee, J.-C.C. Wen, W. Lu, and J. Yang. 2014. Why hydraulic tomography works? *Ground Water* 52, no. 2: 168–172. DOI:10.1111/gwat.12129.

Yeh, T.-C.J., and C.-H. Lee. 2007. Time to change the way we collect and analyze data for aquifer characterization. *Ground Water* 45, no. 2: 116–118. DOI:10.1111/j.1745–6584.2006.00292.x.

Yeh, T.-C.J., and S. Liu. 2000. Hydraulic tomography: Development of a new aquifer test method. *Water Resources Research* 36, no. 8: 2095–2105. DOI:10.1029/2000WR900114.

Zhu, J., and T. Yeh. 2005. Characterization of aquifer heterogeneity using transient hydraulic tomography. *Water Resources Research* 41, no. 7: 1–10. DOI:10.1029/2004WR003790.